AIAA AVIATION Forum
June 27-July 1, 2022, Chicago, IL & Virtual
AIAA AVIATION 2022 Forum

10.2514/6.2022-3600

A Fully-Coupled Computational Aeroelasticity Model for Transonic and Supersonic Flows

Marcel Ilie[1] and John Havenar[2]
Georgia Southern University, Statesboro, GA, 30458

The aeroelastic phenomena of fixed-wing aircraft in transonic and supersonic flight regimes plays a critical role in the design of high-speed aircraft. The present research concerns the development of computationally efficient and accurate methods for the computation of aeroelastic systems containing transonic and supersonic flows. Therefore, we propose a fully-coupled, time-marching aeroelastic approach utilizing an URANS model. The computational studies are carried out to assess the effect of the freestream Mach number and angle of attack on the structural dynamics and stresses developed in the wing structure. The studies are carried out for a range of Mach numbers, $M_\infty = 0.8 - 1.4$, and angles of attack, $\alpha = \{2°, 4°, 6°\}$. The analysis reveals that the aeroelastic deformation of the wing and induced stress in the wing structure increase with the freestream Mach number.

I. Introduction

Aeroelasticity is encountered in many engineering applications and poses interest and challenges, equally. Aeroelasticity is a phenomenon of particular interest in the aerospace industry since it affects the aerodynamic performance of the aircraft. Good prediction of the aeroelastic effects in high-speed flight regimes would ensure good aerodynamic performance and aircraft safety. Experimental studies of aeroelasticity are challenging and costly. Therefore, the computational approaches are a promising alternative for the prediction of aeroelastic effects. However, the computational aeroelasticity of high-speed flows such as transonic and supersonic flows pose significant challenges mainly due to the computational cost and approaches employed. Most of the studies use two separate solvers, one for the fluid flow and another one for the structural dynamics. This approach may lead to erroneous predictions of the aeroelastic effects.

Usually, the fluid flow is computed using computational fluid dynamics (CFD), employing either finite-difference or finite-volume methods (FVM), while the structure is usually computed using a finite element method (FEM). The coupling between the two solvers ensures the full-coupling of the fluid and structure. A data-passing service couples these systems together by sending surface forces from the CFD solver to the finite element analysis (FEA) solver and returning incremental displacements from the FEA solver to the CFD solver.

In order to obtain a robust solution while using a transient simulation approach, a staggered iterative loop may be used. For strongly coupled fluid-structure interaction problems, it is common for the viscous flow regime to be resolved using unsteady Reynolds-averaged Navier-Stokes (URANS) equations rather than the large eddy simulation (LES), scale adaptive simulation (SAS), and detached eddy simulation (DES) approaches due the high CPU time costs that are incurred when they are paired with a staggered, time-marching approach.

The purpose of this work is to investigate the aeroelastic response of an aircraft wing for varied angles of attack and flow velocities. By observing the induced oscillating stresses and displacements in the structural domain over several angles of attack for various freestream flow velocities, a relationship between the freestream Mach number and the induced dynamic aeroelastic response may be characterized. This work also serves reinforce the continually growing body of literature which makes use of commercial CFD and FEA codes for modeling complex, unsteady aeroelastic phenomena.

The main goal of this research is to study the aeroelastic effect on the aerodynamic performance of high-speed fixed wing aircraft. The focus on aerodynamic performance and efficiency of planes and spacecraft have been at the forefront of the aerospace industry since the beginning of its existence. The lift and drag of airfoils have been extensively studied to determine the optimum shape and angle of attack (AoA) to generate sufficient lift. As an airfoil reaches its critical AoA, where lift is maximized, a pressure gradient causes the flow to detach from the surface. The

[1] Assistant Professor, Department of Mechanical Engineering
[2] Undergraduate Student, Department of Mechanical Engineering

phenomenon known as flow separation occurs causing a decrease in lift and an increase in drag. The present studies concern the effect of the aeroelastic on the flow separation and aerodynamic performance.

II. Computational method and models

The present study used a swept wing having a NACA 4412 airfoil with a chord length of 1.84 meters and a span of 3.09 meters. The near-wing region and boundary layer mesh is shown in Fig. 1.

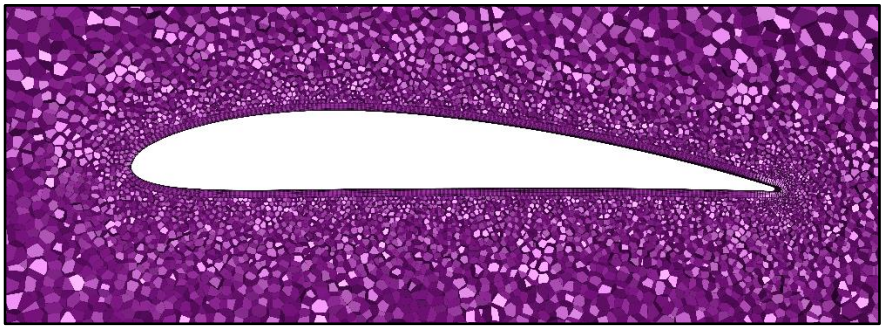

(a) Near wing mesh at wing base.

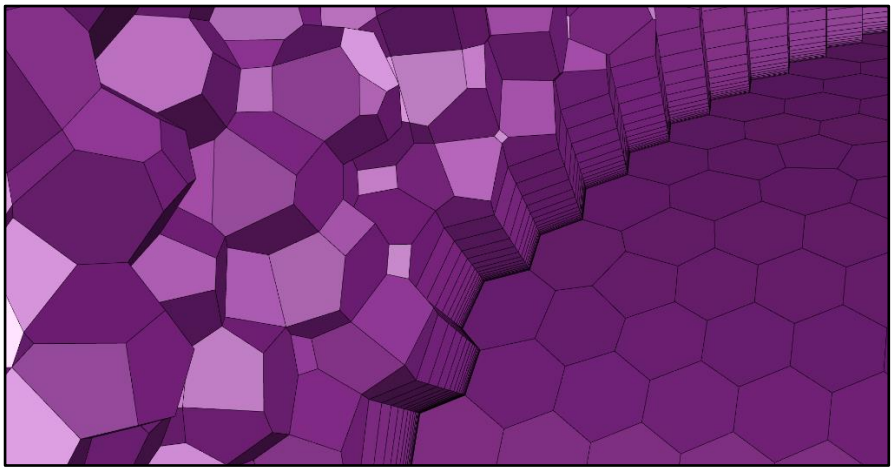

(b) Surface meshing and boundary layer resolution.

Fig. 1. The computational domain for the aeroelastic analysis of the swept wing.

In the present work, an unsteady Reynolds-averaged Navier-Stokes (RANS) model is used for the computation of the turbulent flow field enveloping the wing and a linearly elastic structural dynamics method is utilized for the deformation of the wing structure.

The fluid domain was discretized using an unstructured polyhedral meshing scheme with volume refinement near the wing geometry for resolution of wake vorticity [1]. Prism layers were extruded as shown in Fig. 1b from the wing surface mesh to resolve the turbulent boundary layer. The wing structure was meshed with a quadratic tetrahedral scheme with surface sizing equivalent to that of the wing surface in the fluid continuum. The computational fluid domain consists of 4.9 million cells and 20.6 million nodes.

The freestream Mach number was varied between 0.80 and 1.40. A time step of 5×10^{5} seconds was selected for the analyses. The turbulent flow field was computed using a finite volume method Navier-Stokes equation solver with the unsteady k-ω SST viscous model, a two-equation eddy-viscosity model capable of accurate prediction of flows with strong adverse pressure gradients and pronounced turbulence features, namely separation and reattachment [2-4]. The k-ω SST model was additionally selected for its promise in transonic buffet prediction when implemented in its unsteady formulation [5].

Within the k-ω SST model, the equations for turbulent kinetic energy and the turbulent dissipation rate are expressed in the conservation form as given by Eq. (1) and Eq. (2), respectively.

$$\frac{\partial(\rho k)}{\partial t}+\frac{\partial(\rho U_i k)}{\partial x_i}=\tilde{P}_k-\beta^*\rho k\omega+\frac{\partial}{\partial x_i}\left[(\mu+\sigma_k\mu_t)\frac{\partial k}{\partial x_i}\right] \tag{1}$$

$$\frac{\partial(\rho\omega)}{\partial t}+\frac{\partial(\rho U_i \omega)}{\partial x_i}=\alpha\rho S^2-\beta\rho\omega^2+\frac{\partial}{\partial x_i}\left[(\mu+\sigma_\omega\mu_i)\frac{\partial\omega}{\partial x_i}\right]+2(1-F_1)\rho\sigma_{w2}\frac{1}{\omega}\frac{\partial k}{\partial x_i}\frac{\partial\omega}{\partial x_i} \tag{2}$$

To avoid instabilities stemming from freestream turbulent parameters, the model uses blending function given by Eq. (3) to transition from the k-ω formulation in the boundary layer to a k-ε model behavior in the freestream flow, where $CD_{k\omega}$ as expressed in Eq. (4) is the positive component of the cross-diffusion term of the turbulent dissipation equation in Eq. (2).

$$F_1=\tanh\left\{\left\{min\left[max\left(\frac{\sqrt{k}}{\beta^*\omega y},\frac{500v}{y^2\omega}\right),\frac{4\rho\sigma_{\omega 2}k}{CD_{k\omega}y^2}\right]\right\}^4\right\} \tag{3}$$

$$CD_{kw}=max\left(2\rho\sigma_{\omega 2}\frac{1}{\omega}\frac{\partial k}{\partial x_i}\frac{\partial\omega}{\partial x_i},10^{-10}\right) \tag{4}$$

The kinematic eddy viscosity, ν_t, is given in Eq. (5) and utilizes an additional blending function, F_2, to scale the vorticity magnitude. The second blending function is given in Eq. (6).

$$\nu_t=\frac{a_1 k}{max(a_1\omega,SF_2)} \tag{5}$$

$$F_2=\tanh\left[\left[max\left(\frac{2\sqrt{k}}{\beta^*\omega y},\frac{500v}{y^2\omega}\right)\right]^2\right] \tag{6}$$

To prevent undo excess turbulence in stagnation regions, the turbulence production, P_k, as expressed in Eq. (7), is limited according to the criteria in Eq. (7).

$$P_k=\mu_t\frac{\partial U_i}{\partial x_j}\left(\frac{\partial U_i}{\partial x_j}+\frac{\partial U_j}{\partial x_i}\right),\qquad \tilde{P}_k=min(P_k,10\cdot\beta^*\rho k\omega) \tag{7}$$

The closure constants are: β^*=0.09, α_1=5/9, β_1=3/40, σ_{k1}=0.85, $\sigma_{\omega 1}$=0.5, α_2=0.44, β_2=0.0828, σ_{k2}=1, $\sigma_{\omega 2}$=0.856. To ensure the proper resolution of turbulent flow structures and their effects on the wing surface loading, all equations were solved to second order accuracy with a bounded second order implicit transient formulation used to govern the global time-marching of the fluid model.

A no-slip wall was used as the wing surface. A pressure far-field boundary with the freestream Mach number, $\boldsymbol{M}_\infty$, specified as requisite characteristic information was imposed a radial distance of $r=30c_r$ from the wing structure [6].

The fluid mesh dynamically adapted to the aeroelastic deformation of the wing structure via a diffusive smoothing method. The diffusive smoothing method used a diffusion coefficient which was a function of a normalized boundary distance in order to shift the burden of mesh motion away from the highly-sensitive near-wall region [7].

The governing Laplace equation for the mesh motion and the formulation of the diffusion coefficient, γ, where $0 \le \alpha \le 2$, are given as Eq. (8).

$$\nabla\cdot(\gamma\nabla\vec{u})=0,\qquad \gamma=\frac{1}{d^\alpha} \tag{8}$$

The wing structure was treated as a linearly elastic structural continuum and the deformation was computed with a finite element method (FEM). The wing structure dynamics were computed the beta-Newmark time-integration algorithm, a single-step time integration algorithm proven effective for the computation of structural dynamics with transient surface loading [8].

III. Results and Discussion

The velocity field given in Fig. 2 near the wing body at $\boldsymbol{M}_\infty$ = 0.80 and 2° and 6° of incidence reveals the increase of the flow separation with the increase of the angle of attack. The flow separation causes a displacement of the shock, while concentrating the shock in a more confined region.

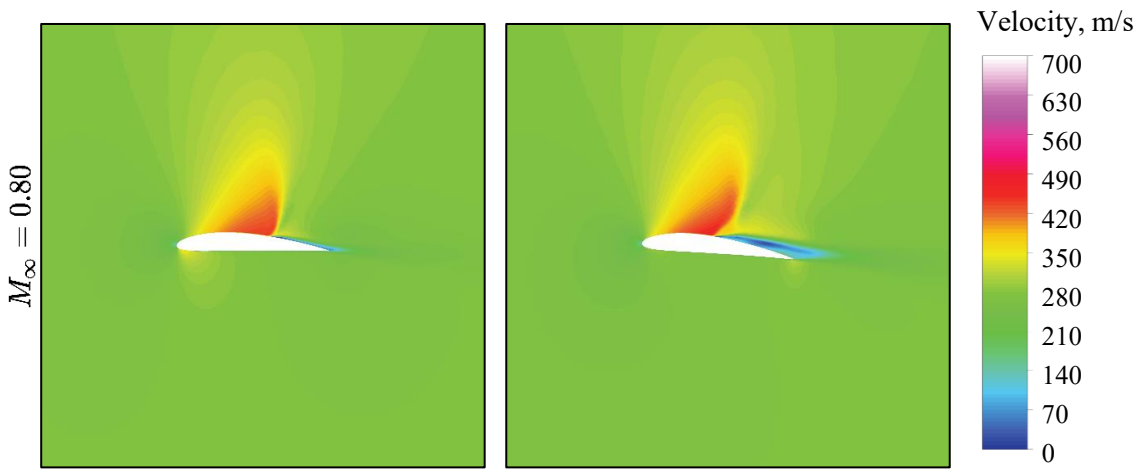

(a) AoA = 2° **(b) AoA = 6°**

Fig. 2. Velocity field vs. AoA.

Analysis of the pressure field reveals that the stagnation point is located below the leading-edge, on the lower surface of the wing. The increase of the Mach number causes an increase of the pressure on the lower surface. Pressure waves radiating from the lower surface of the wing are observed as well. The magnitude of the pressure waves increases with the Mach number. The unsteady pressure fluctuations at the surface of the wing cause a time-dependent lift coefficient, as shown in Figure 3.

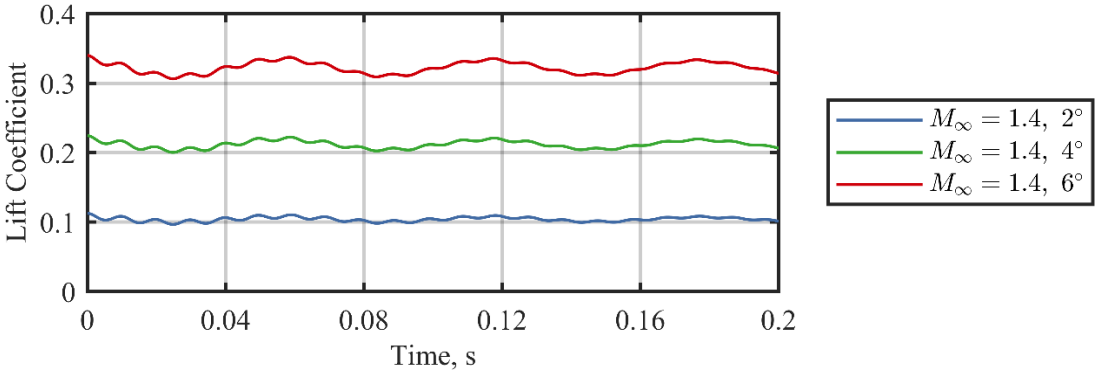

Fig. 3. Lift coefficient fluctuations resulting from transient pressure waves.

Figure 4 presents the pressure field for two angles of attack at $\boldsymbol{M}_\infty$ = 0.80. The study reveals that the high-pressure region expands with an increase of angle of attack.

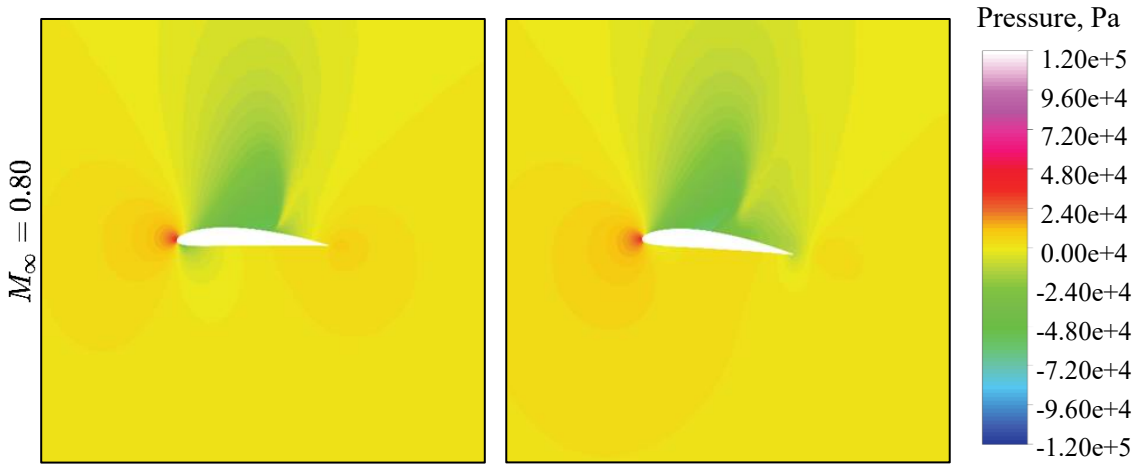

(a) AoA = 2° **(b) AoA = 6°**

Fig. 4. Pressure field vs. AoA.

However, a relatively large pressure region is observed beneath the airfoil for AoA = 2°, while for AoA = 6°, the high-pressure region is located at the upper surface of the airfoil, and it extends towards the trailing-edge. The high-pressure region below the airfoil for AoA = 2° is due to camber of the airfoil.

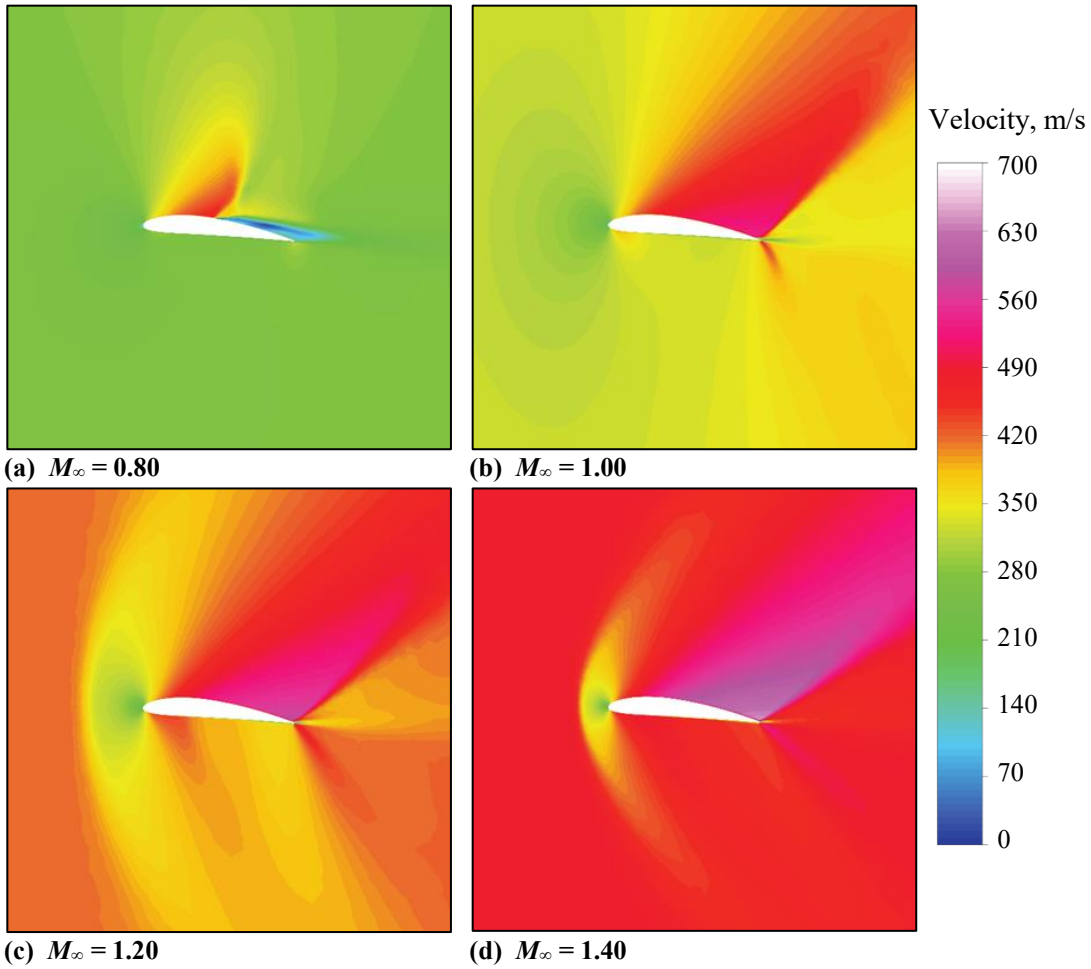

(a) $M_\infty = 0.80$ **(b) $M_\infty = 1.00$**

(c) $M_\infty = 1.20$ **(d) $M_\infty = 1.40$**

Fig. 5. Mach number effect for AoA = 6°.

Figure 5 presents the Mach number effect on the flow field for an angle of attack AoA = 6°. The analysis shows that the Mach number has a significant impact on the flow field. Thus, the increase of the Mach number generates different flow configurations. For a transonic regime $\boldsymbol{M}_\infty$ = 0.80, there is a flow separation that expands the second-half of the airfoil. With the increase of the Mach number to $\boldsymbol{M}_\infty$ = 1.00, there is no flow separation. However, shock waves are present at the trailing-edge. A well-defined region of shock waves is observed in the leading-edge region as well. Further increase of the Mach number causes an increase of the pressure at the region ahead of the leading-edge, which is the bow shock. Shock waves are also observed along the airfoil, for both upper and lower surfaces. Strong shock waves are observed at the trailing-edge as well. Further increase of the Mach number causes the bow shock to be confined to a smaller region with higher strength.

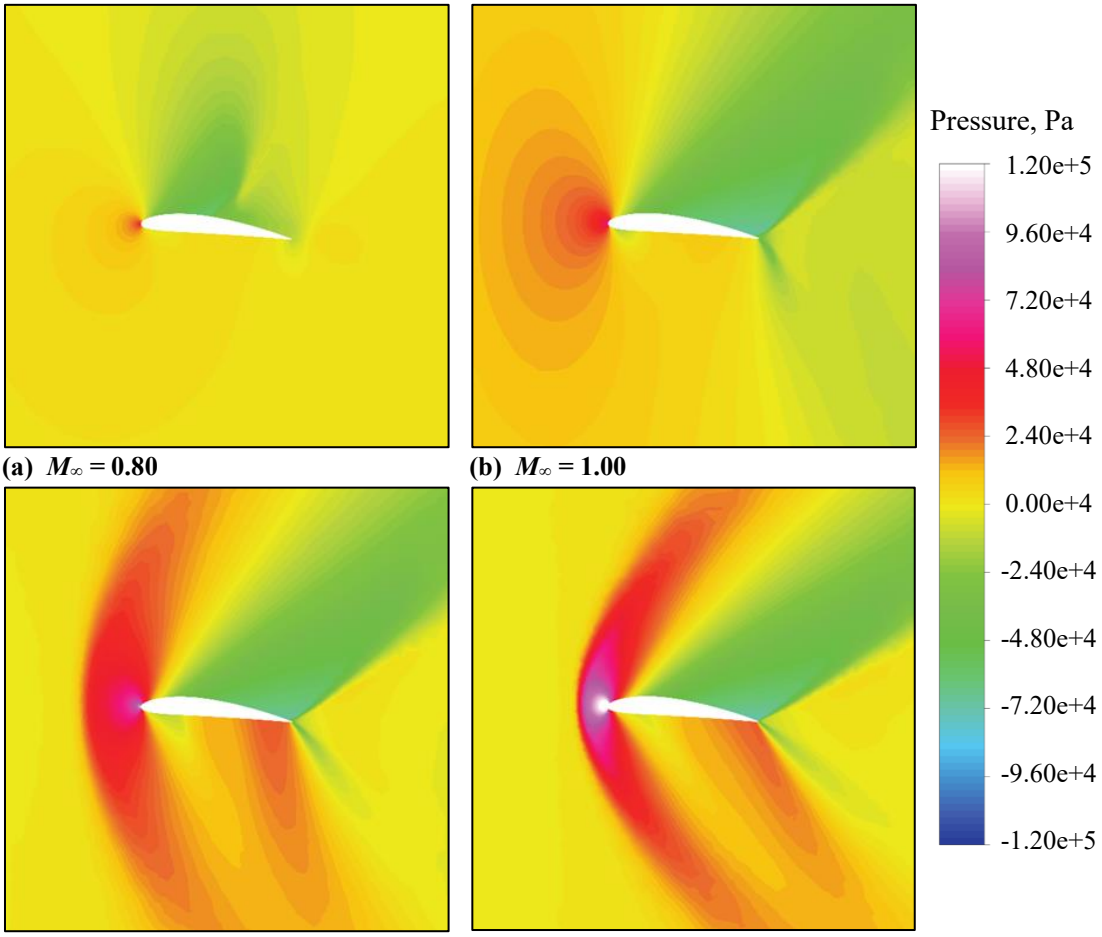

(a) M_∞ = 0.80 **(b) M_∞ = 1.00**

(c) M_∞ = 1.20 **(d) M_∞ = 1.40**

Fig. 6. Pressure field variation for AoA = 6°.

Figure 6 presents the pressure field variation with the Mach number for AoA = 6°. The analysis reveals an overall pressure increase with the Mach number. Also, the pressure distribution exhibits different characteristics with the increase of Mach number. Thus, for sonic flow, $\boldsymbol{M}_\infty$ = 1.00, pressure waves are observed ahead of the leading-edge the airfoil. Lower pressure is observed behind the shock waves. As the Mach number increases, the pressure field increases and thus, a stronger shock is observed for Mach number $\boldsymbol{M}_\infty$ = 1.20. For Mach number $\boldsymbol{M}_\infty$ = 1.20, shocks are formed at the trailing-edge of the airfoil as well, as shown in Fig. 6c. For $\boldsymbol{M}_\infty$ = 1.40, the shocks further increase in intensity at both leading and trailing-edges.

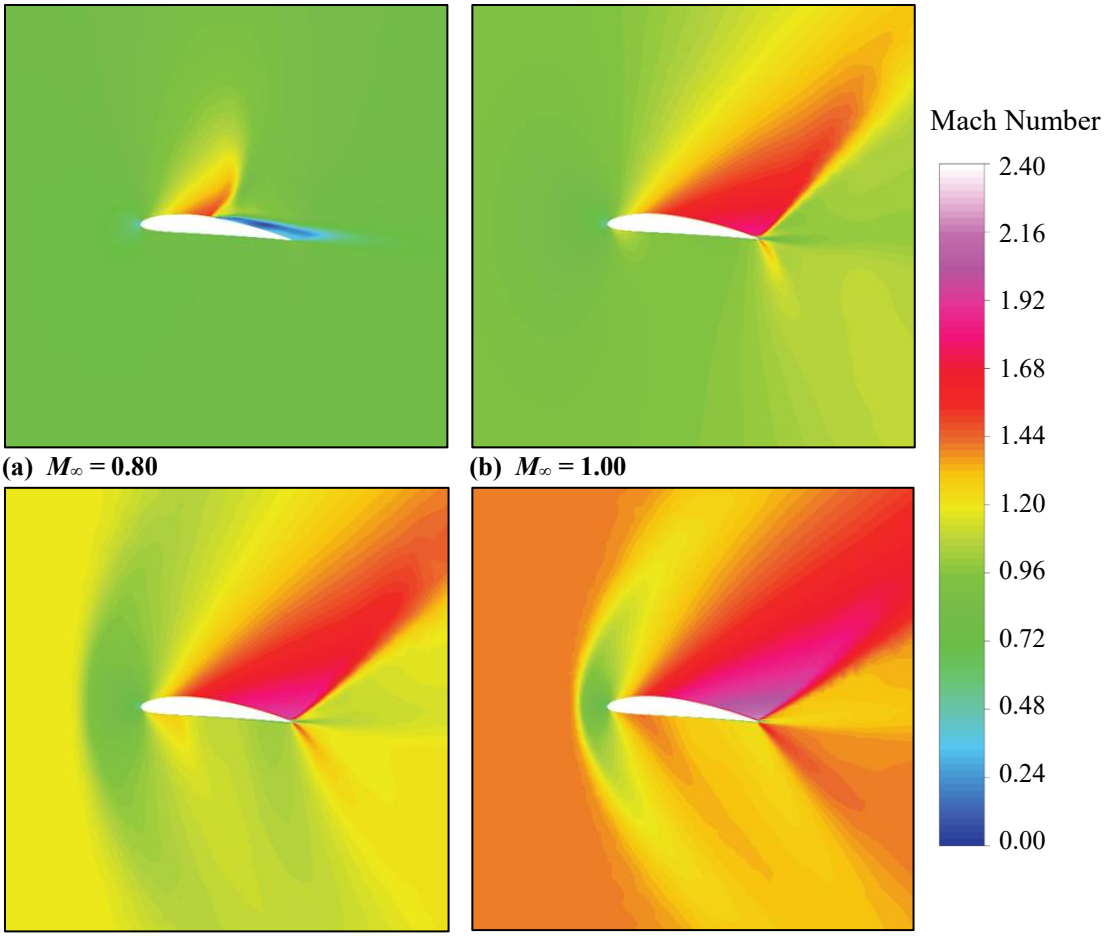

Fig. 7. Mach number distribution for AoA = 6°.

Figure 7 presents the distribution of the Mach number for AoA = 6° and four different freestream flow velocities. Similar to the velocity field, the Mach number field exhibits high values with an increase of flow speed. The analysis of the Mach number also reveals the presence of shocks whose strength increases with the Mach number.

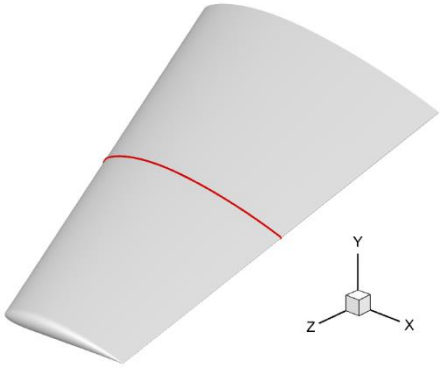

Fig. 8. Schematic of interrogation line 1.

Figure 8 presents the interrogation line 1, where the fluid and structural dynamics of the wing is analyzed. Line 1 is located at the mid-span of the wing.

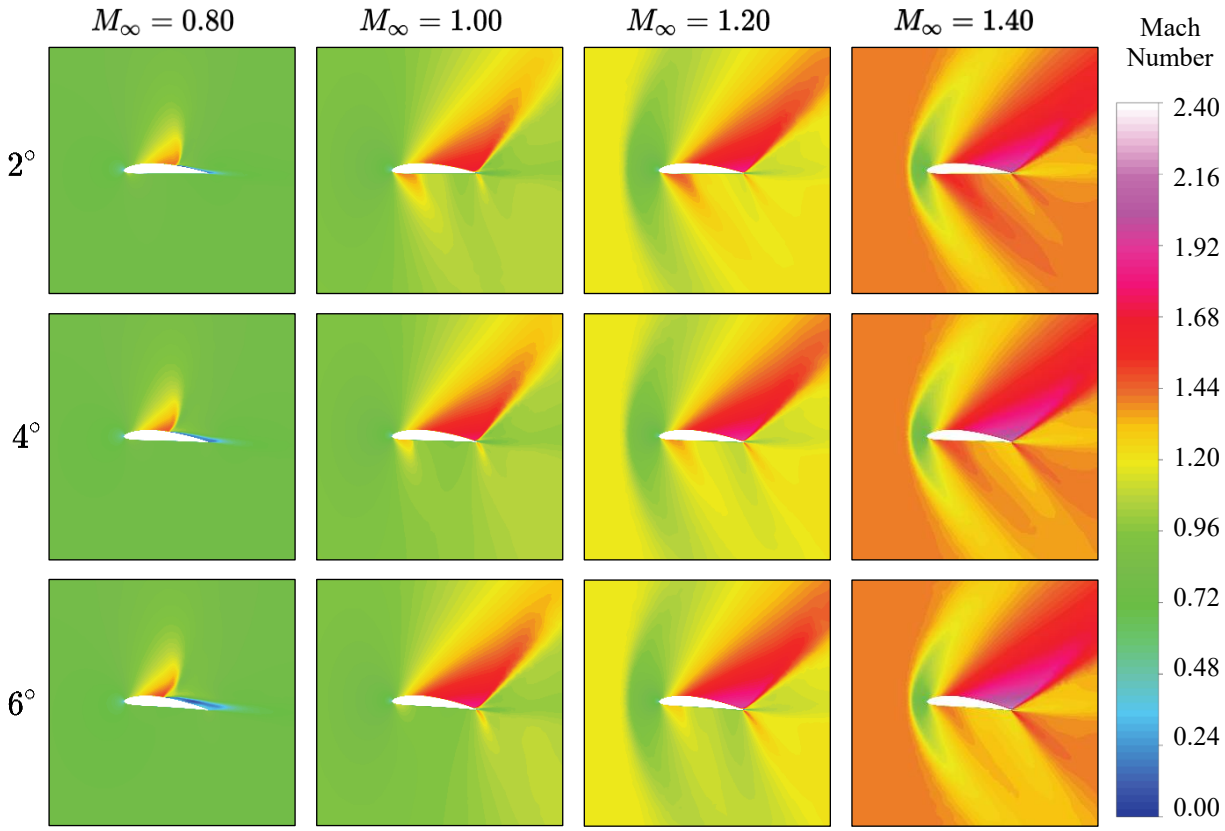

Fig. 9. Mach number contours at interrogation line 1.

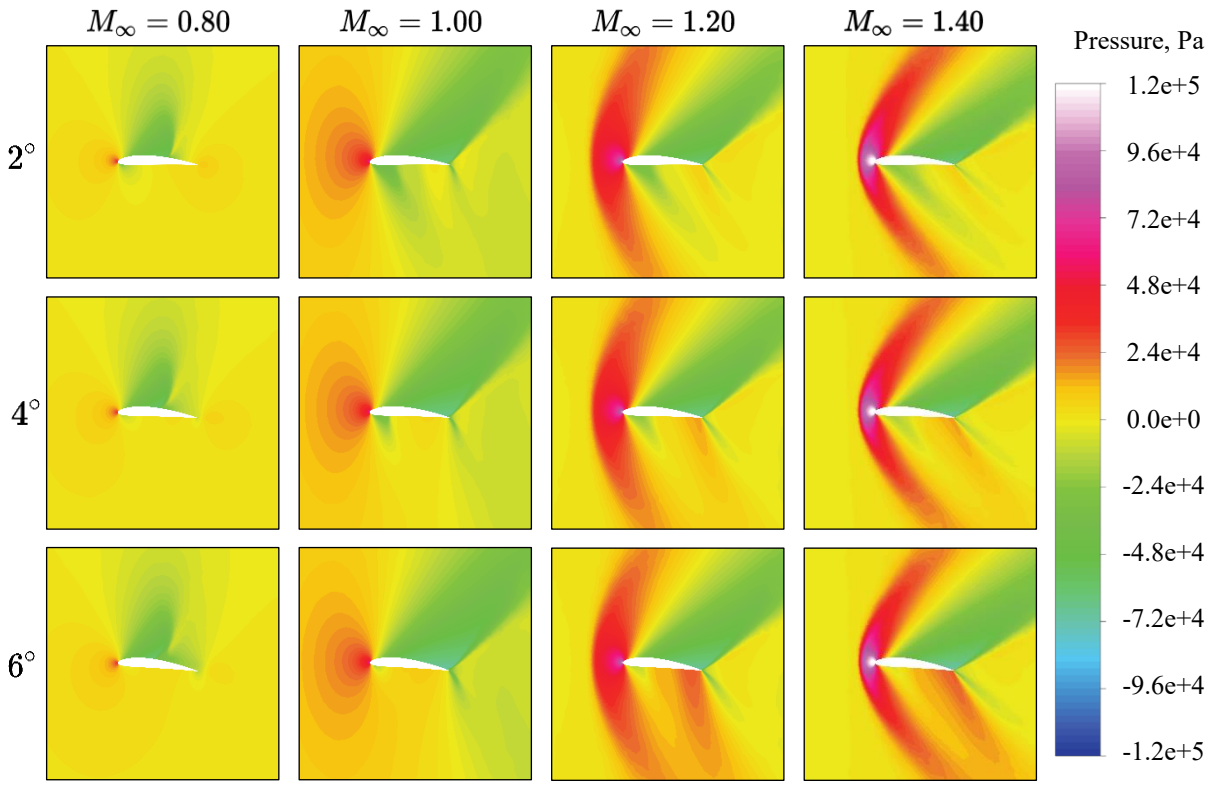

Fig. 10. Pressure contours at interrogation line 1.

Figure 9 presents the variation of the Mach number with the angle of attack. The analysis of Mach number contours shows the increase in local Mach number with the angle of attack. Two oblique shocks are observed in the case of the transonic flow, one at the leading-edge and the other one at the trailing-edge. The increase of the Mach number causes a bow shock ahead of the wing. String shocks are observed at the trailing-edge of the wing. The variation of the Mach number is also reflected onto the pressure field. Therefore, an increase of pressure with the Mach number is also observed.

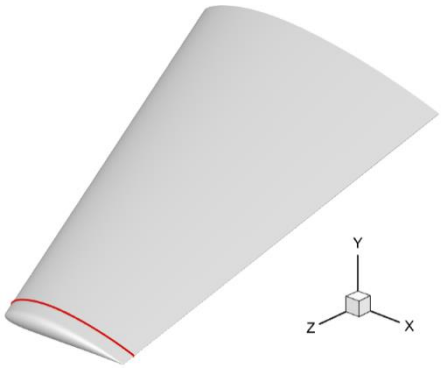

Fig. 11. Schematic of interrogation line 2.

Figure 11 presents the schematic of the interrogation line 2, located at the tip of the wing. Figure 12 presents the variation of the Mach number with the angle of attack, at the tip of the wing. The analysis shows that the Mach number exhibits lower values at the tip of the wing compared with the values at the mid-span of the wing.

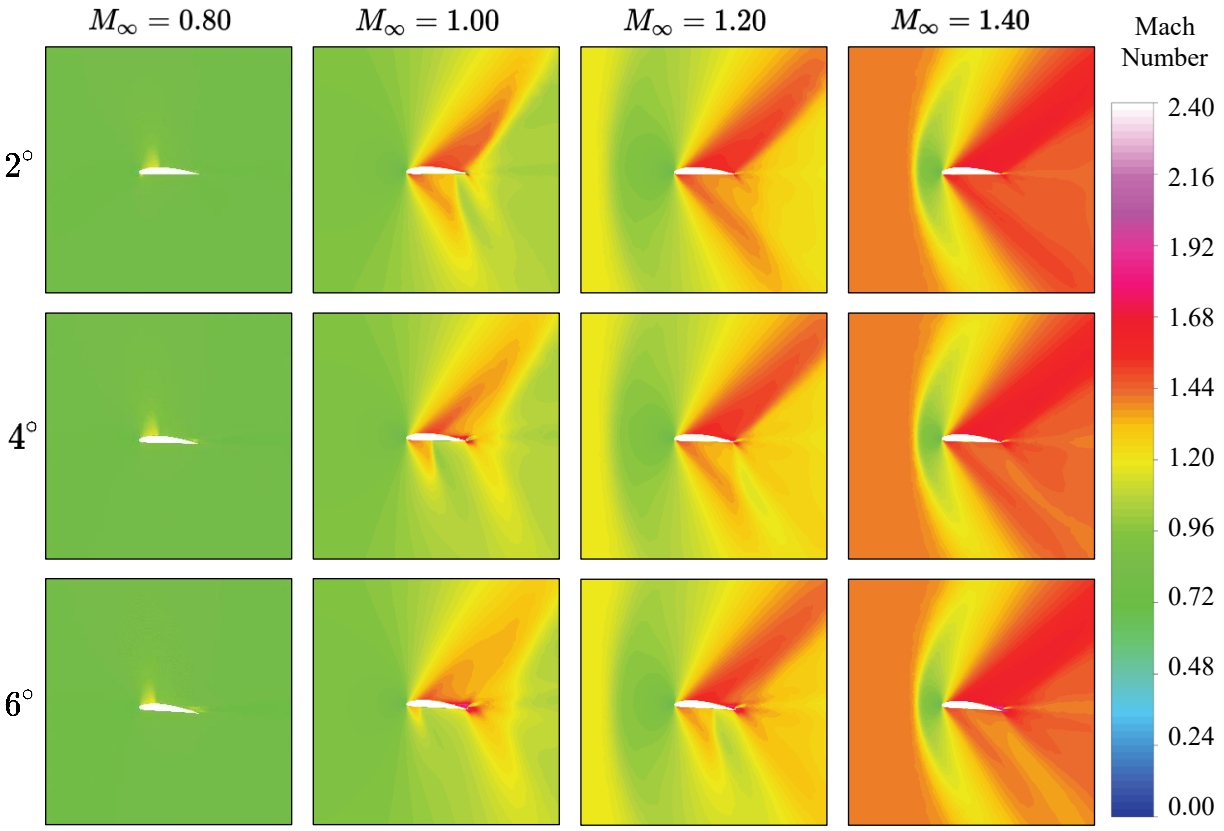

Fig. 12. Mach number contours at interrogation line 2.

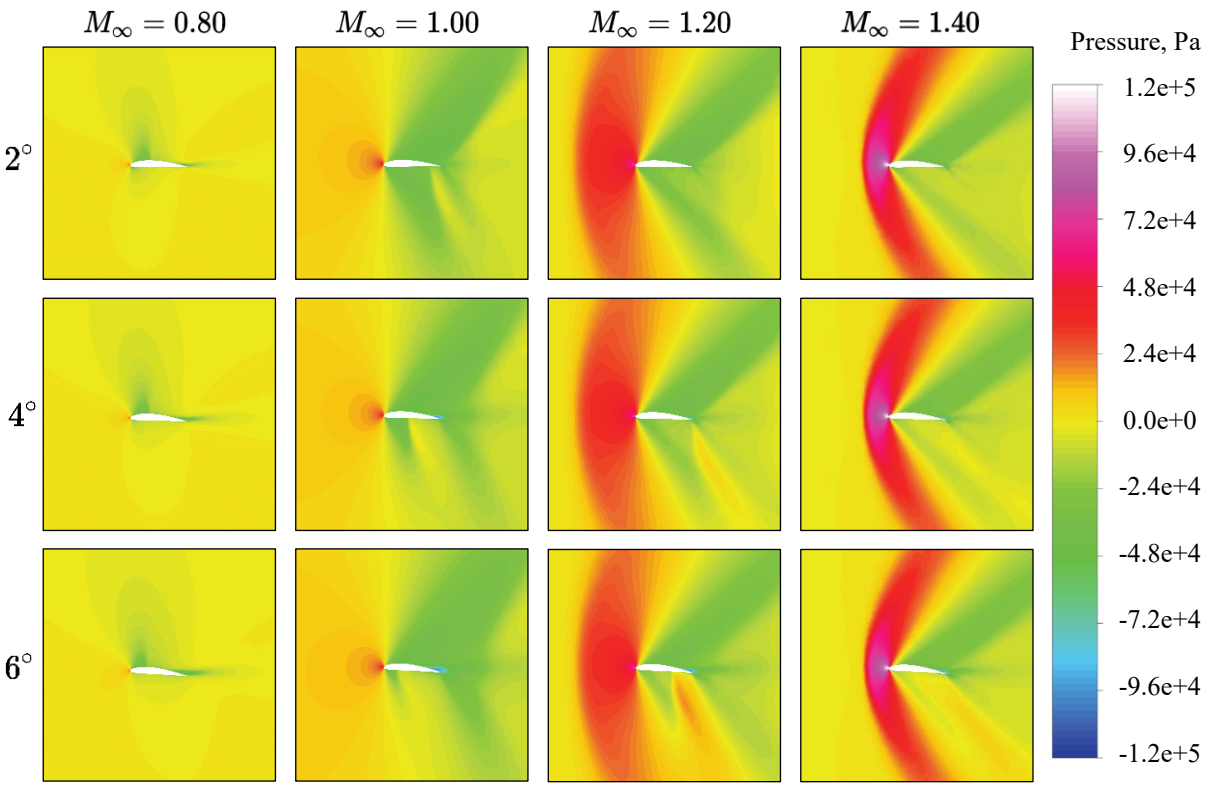

Fig. 13. Pressure contours at interrogation line 2.

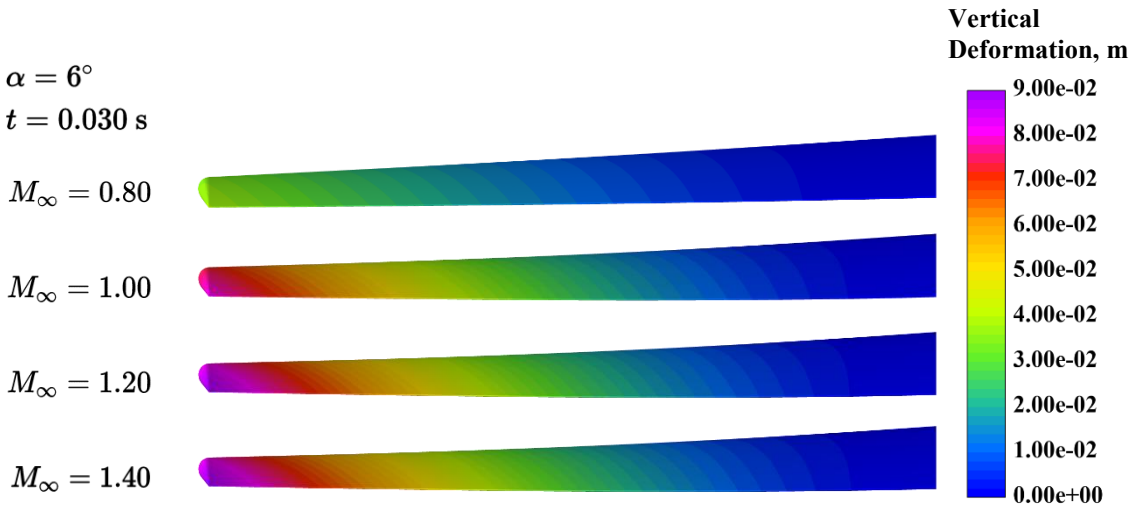

Fig. 14. Vertical deflection along the wingspan.

The vertical deflection along the span increases with the freestream Mach number, as is shown in Fig. 14. There is also an induced aeroelastic twist, as can be seen by the concentration of the deflection towards the intersection of the tip chord and trailing-edge of the wing.

Figure 15 presents the effect of the Mach number on the equivalent stress throughout the wing structure. Both the upper and lower surfaces of the wing are subject to high induced equivalent stress. The analysis reveals an increase of the induced equivalent stress with an increase of the Mach number. This is especially prevalent in the transition from $\boldsymbol{M}_\infty$ = 0.80 to $\boldsymbol{M}_\infty$ = 1.00 as the wing exits the transonic regime.

The increase of equivalent stress corresponding with an increase in the freestream Mach number is constant, however, independent of the freestream Mach number, the wing experiences the highest stress in the hub region, while the tip of the wing presents the lowest stresses.

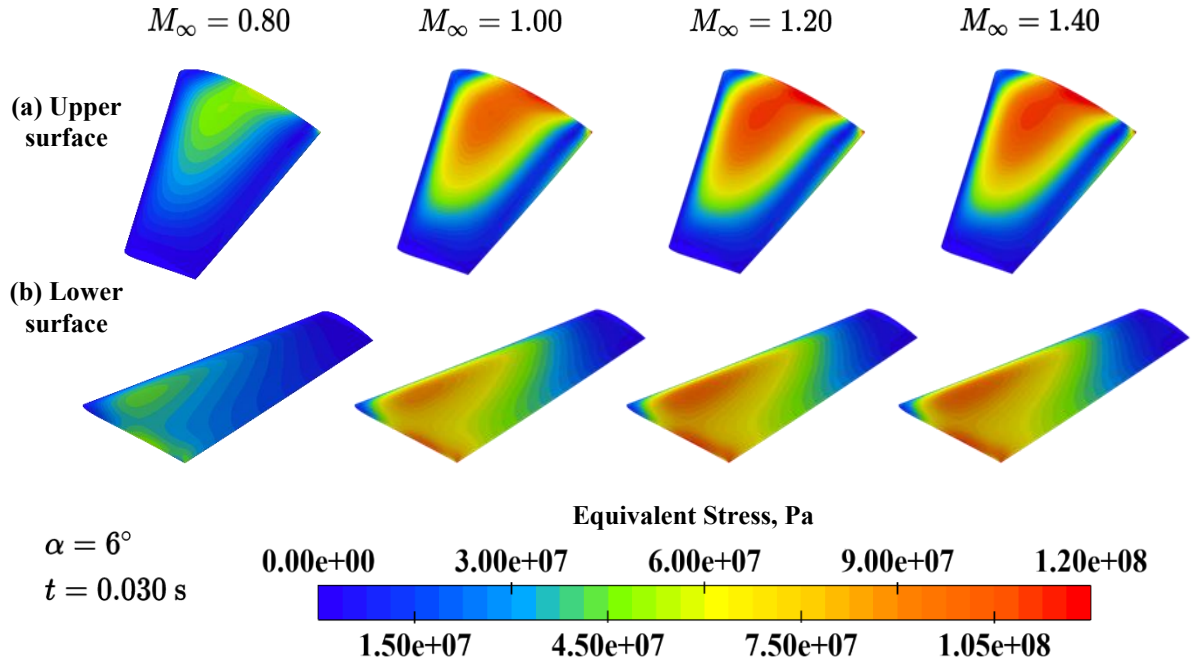

Fig. 15. Equivalent stress over the wing surfaces.

Consideration of the normal stresses presented in Fig. 16 shows that the wing surfaces experience fluctuating tension and compression as the wing experiences the wingtip oscillation which characterizes its aeroelastic response.

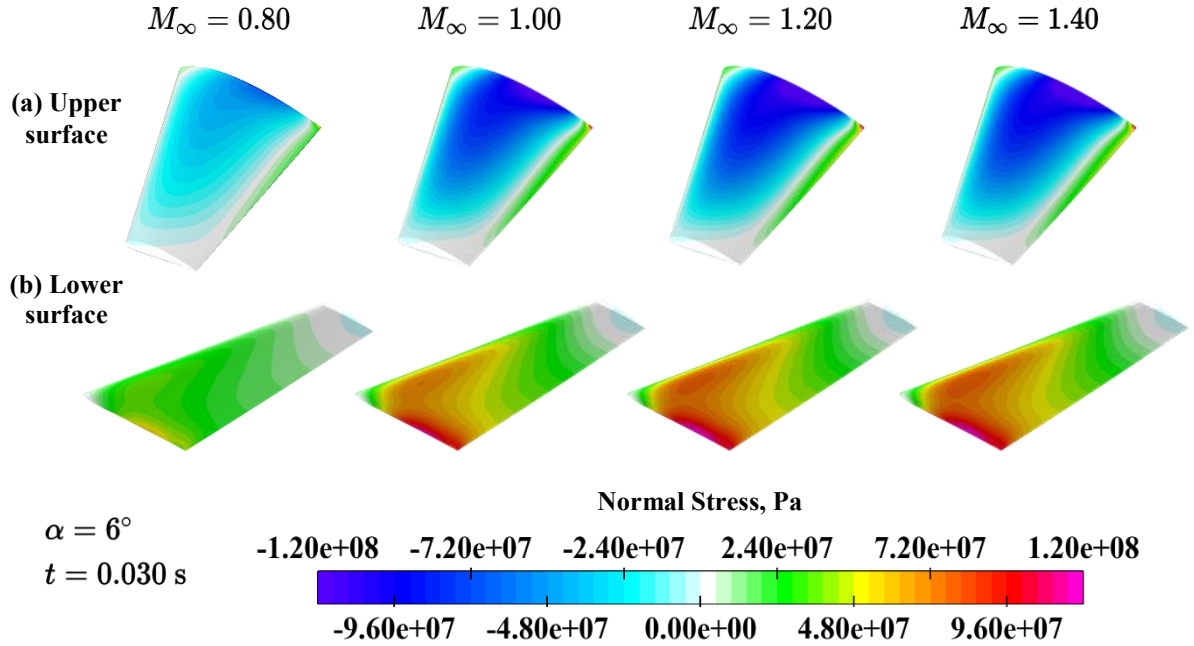

Fig. 16. Normal stress over the wing surfaces.

As the wing structure is vertically deflected, primarily via bending along its span, the upper surface of the wing is compressed while the lower surface is subjected to tension in the spanwise direction. In the same manner as the equivalent stress response shown in Fig. 15, the normal stress is greatest in magnitude at the wing root, and this is independent of the freestream Mach number.

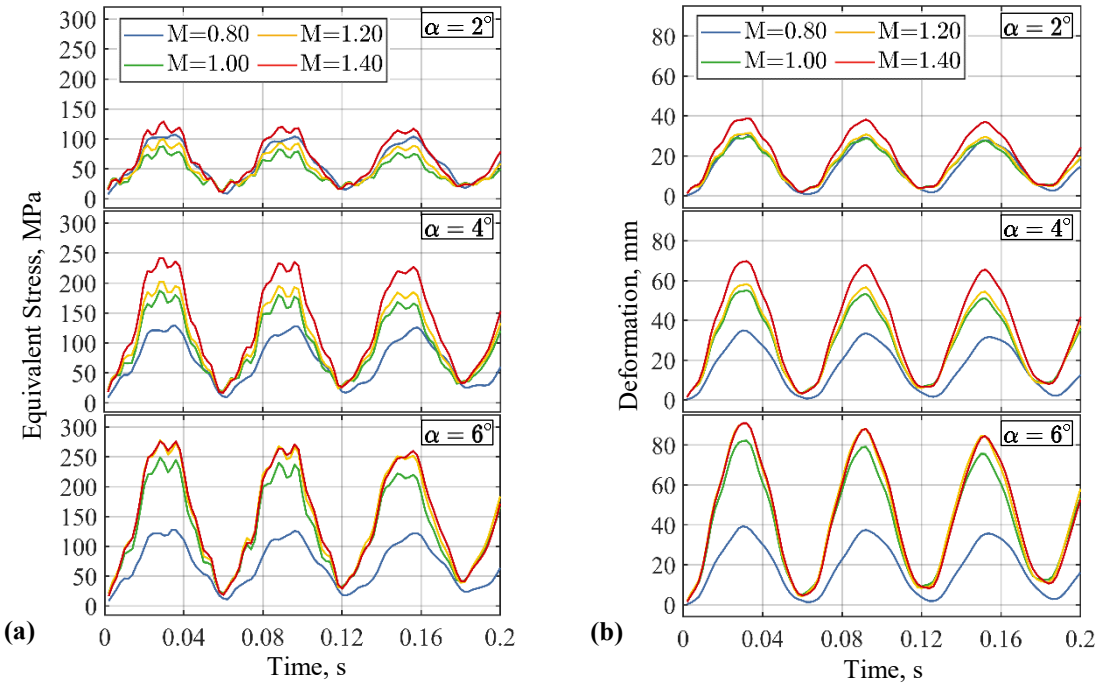

Fig. 17. Structural response of wing over time characterized by: a) wingtip oscillation and b) corresponding equivalent stress.

IV. Conclusions

A fully-coupled computational aeroelasticity model is developed for the prediction of the flow field and structural dynamics of swept wing in the transonic and supersonic regimes. Mach number effect on the aeroelasticity phenomena, of the swept wing, is computationally studied using the fully-coupled aeroelastic method. The flow field is computed using the CFD approach using finite-differences, while the structural analysis is performed using the finite-element method. The study reveals the presence of the bow shock in the transonic and supersonic flight regimes. For supersonic flow, shock waves are present at the trailing-edge. The study shows that the pressure on the lower surface of the wing increases with the Mach number. The elastic deformation and stresses, on the wing, increase with the Mach number. The analysis shows that the upper and lower surfaces of the wing experience alternatively, tensions and compressions.

References

[1] Zore, K., Shah, S., Stokes, J., Sasanapuri, B., and Sharkey, P. "ANSYS CFD Study for High Lift Aircraft Configurations," *2018 Applied Aerodynamics Conference*. 2018.

[2] Menter, F., Kuntz, M., and Langtry, R. B. "Ten years of industrial experience with the SST turbulence model," *Heat and Mass Transfer* Vol. 4, 2003.

[3] Menter, F. R. "Two-equation eddy-viscosity turbulence models for engineering applications," *AIAA Journal* Vol. 32, No. 8, 1994, pp. 1598-1605.
doi: 10.2514/3.12149

[4] Menter, F. "Zonal Two Equation k-w Turbulence Models For Aerodynamic Flows," *23rd Fluid Dynamics, Plasmadynamics, and Lasers Conference*. American Institute of Aeronautics and Astronautics, 1993.
[5] Kumada, K., and Sawada, K. "Improvement in prediction capability of Transonic Buffet on NASA-CRM Using URANS," *54th AIAA Aerospace Sciences Meeting*. 2016.
[6] Jameson, A. "Aerodynamic design via control theory," *Journal of Scientific Computing* Vol. 3, No. 3, 1988, pp. 233-260.
doi: 10.1007/BF01061285
[7] ANSYS. "Fluent User's Guide." ANSYS, Inc., Canonsburg, PA, 2021, pp. 1581-1582.
[8] Newmark, N. M. "A Method of Computation for Structural Dynamics," *Journal of the Engineering Mechanics Division* Vol. 85, No. 3, 1959, pp. 67-94.
doi: 10.1061/JMCEA3.0000098